

**Supplementary Material for
Signatures of odd dynamics in viscoelastic systems:
from spatiotemporal pattern formation to odd rheology**

Carlos Floyd, Aaron R. Dinner, and Suriyanarayanan Vaikuntanathan
The Chicago Center for Theoretical Chemistry, The University of Chicago, Chicago, Illinois 60637, USA
Department of Chemistry, The University of Chicago, Chicago, Illinois 60637, USA and
The James Franck Institute, The University of Chicago, Chicago, Illinois 60637, USA
(Dated: May 16, 2024)

CONTENTS

I. Supplementary Figures	2
II. Supplementary Methods	7
A. Derivation of odd viscoelastic instability threshold	7
B. Simulation methods	10
1. Numerical algorithm	10
2. Initial perturbation	10
3. Parameterization	11
4. Measuring the wavelength	11
III. A microscopic derivation of the viscoelastic dynamical equations	12
References	14

I. SUPPLEMENTARY FIGURES

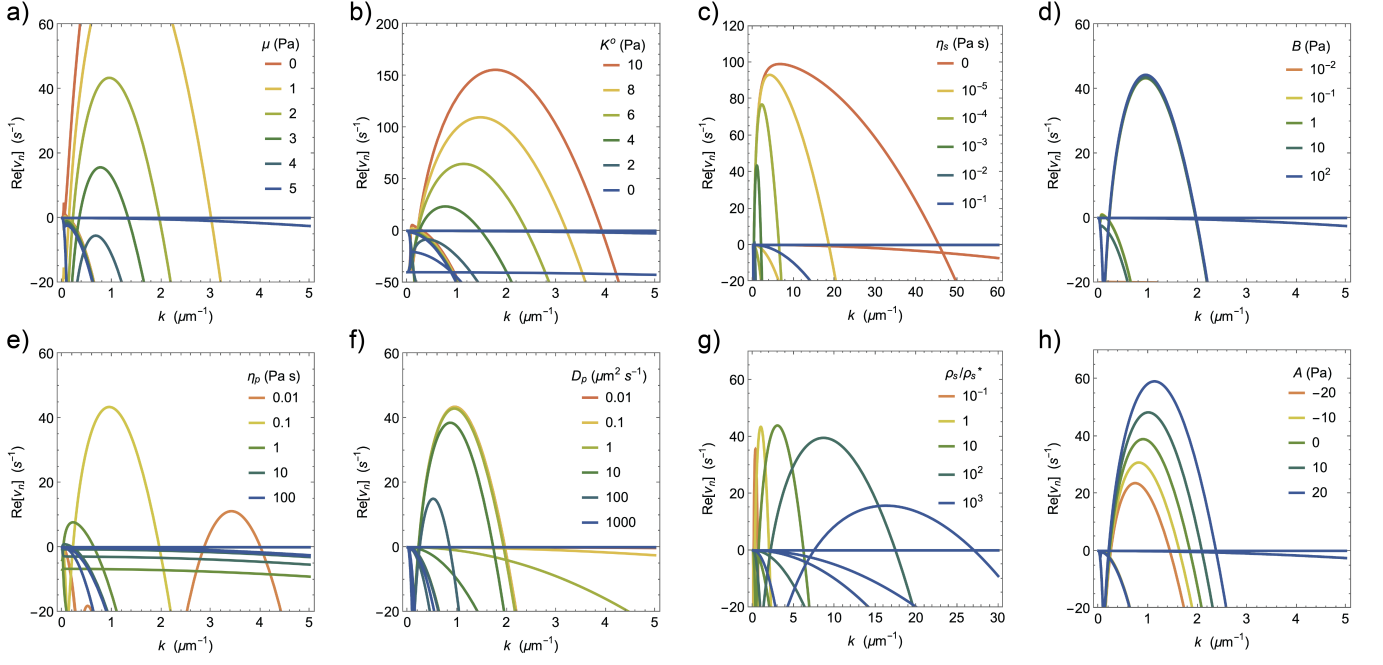


FIG. 1. The dispersion relations as the indicated parameters are varied. The full set of nine solutions $\text{Re}[\nu_n(k)]$ to the dispersion relationship are shown for each condition. The default parameters are listed in Table II below. In panel (g), $\rho_s^* = 2 \times 10^7 \text{ kg/m}^3$.

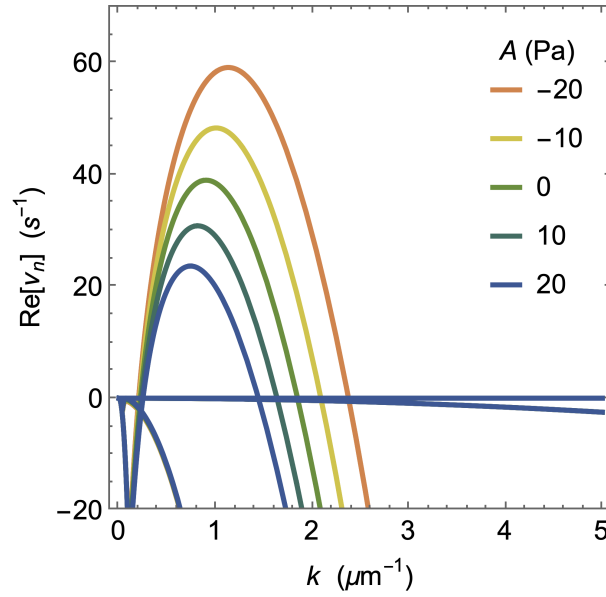


FIG. 2. The solutions $\text{Re}[\nu_n(k)]$ as A is varied, with $K^0 = -5 \text{ Pa}$. See Figure 1h for the corresponding plot when $K^0 = 5 \text{ Pa}$.

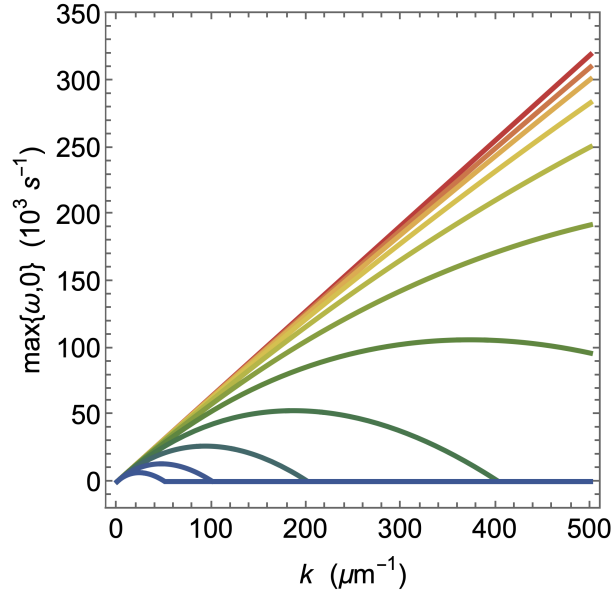


FIG. 3. The function $\max\{\omega, 0\}$ as η_s is varied in the special case considered in Ref. 1, with $K^o = 100$ Pa, $A = 0$ Pa, $\eta_p \rightarrow \infty$ Pa s, and $D_p = 0$ $\mu\text{m}^2/\text{s}$. The remaining parameters are listed in Table II. The red line corresponds to $\eta_s = 0$ Pa s, and the colors range from red to blue as η_s increases by powers of 2 from 10^{-6} to 5.12×10^{-4} Pa s.

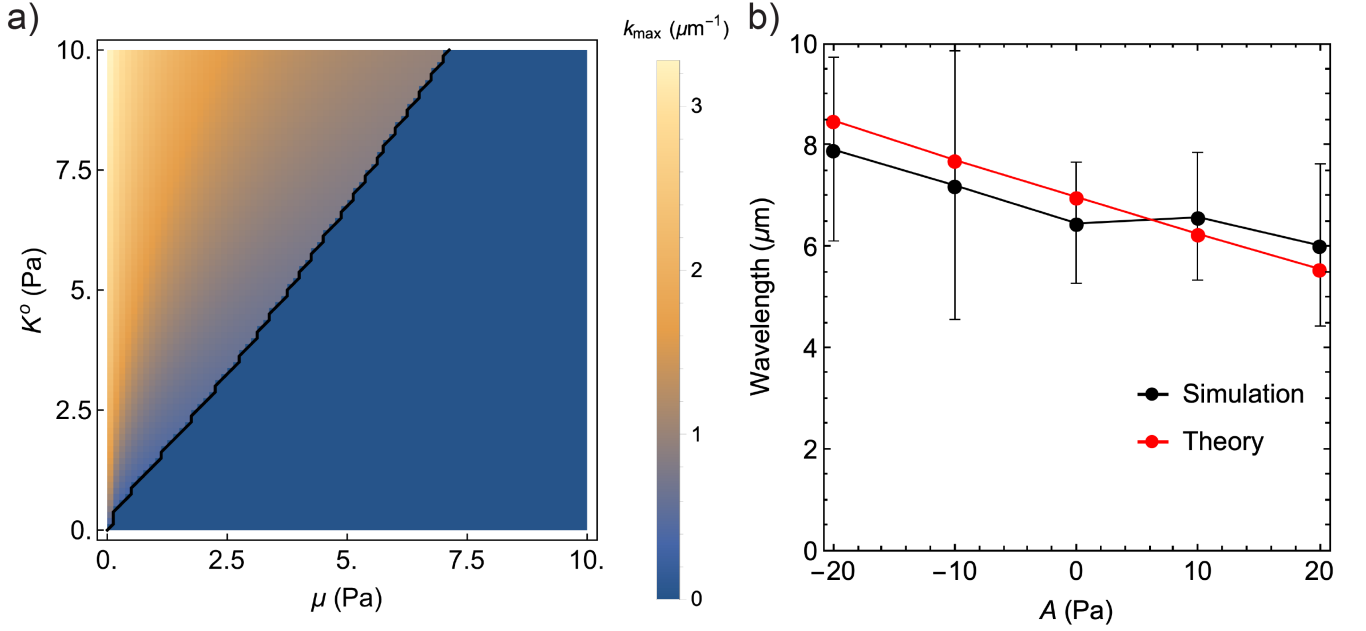


FIG. 4. (a) A heatmap of $\max\{0, k_{\max}\}$ as K^o and μ are varied, with a contour at $\omega_{\max} = 0$ drawn in black. (b) The spatial wavelengths from theory (red points, computed as $2\pi/k_{\max}$) and simulation (black points, see Supplementary Methods for details) as A is varied. The error bars represent the standard deviation over the time interval $[0.13 \text{ s}, 0.16 \text{ s}]$ and 5 trials. We measured the characteristic wavelength of the patterns while varying A by first finding the spatial correlation function of the vorticity field $C_\Omega(r)$, which is oscillatory due to the patterning, and then using the position of the first minimum of $C_\Omega(r)$ as an estimate of half the wavelength (see Supplementary Methods Section IIB for more details). We find that for a given condition the characteristic wavelength has large variations over multiple random initial perturbations (see Supplementary Figure 5), yet it tracks the trends predicted from the analytical theory on average.

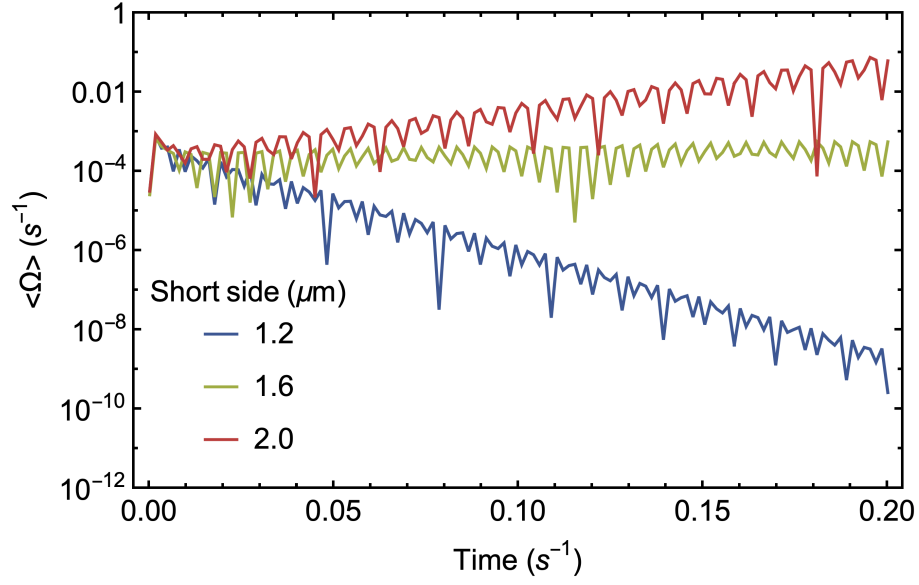


FIG. 5. Suppression of pattern formation from confinement. The average total vorticity $\langle \Omega \rangle \equiv \int |\Omega(\mathbf{r})| d\mathbf{r} / \int d\mathbf{r}$ is shown as the short side of the simulation domain is varied. The long side of the domain is $16 \mu m$, and the remaining parameters are the default ones.

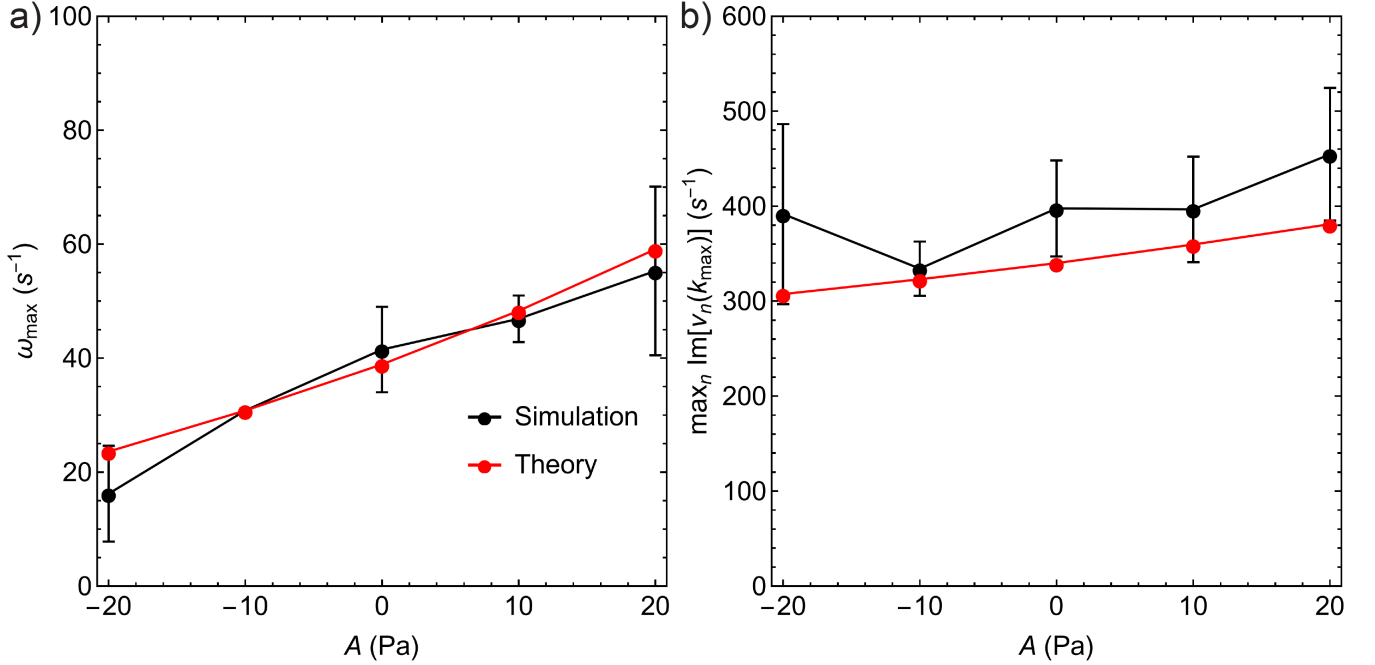


FIG. 6. (a) Comparison of ω_{\max} between simulation and theory as A is varied. To estimate ω_{\max} from simulation we fit the functional form in Equation 6 of the main text to the vorticity at a fixed point in space. See Figure 4 of the main text for plots of these curves and the corresponding fits. ω_{\max} is estimated from the parameter b of these fits. The standard deviation over five trials is represented as error bars for each value of A . (b) Comparison of the oscillation frequency between simulation and theory as A is varied. In the theory, we estimate the oscillation frequency as the maximum imaginary part of the frequency evaluated at k_{\max} , i.e., $\max_n \text{Im}[\nu_n(k_{\max})]$, and in simulation we estimate it as the fitting parameter c in Equation 6 of the main text. Error bars are as in panel (a).

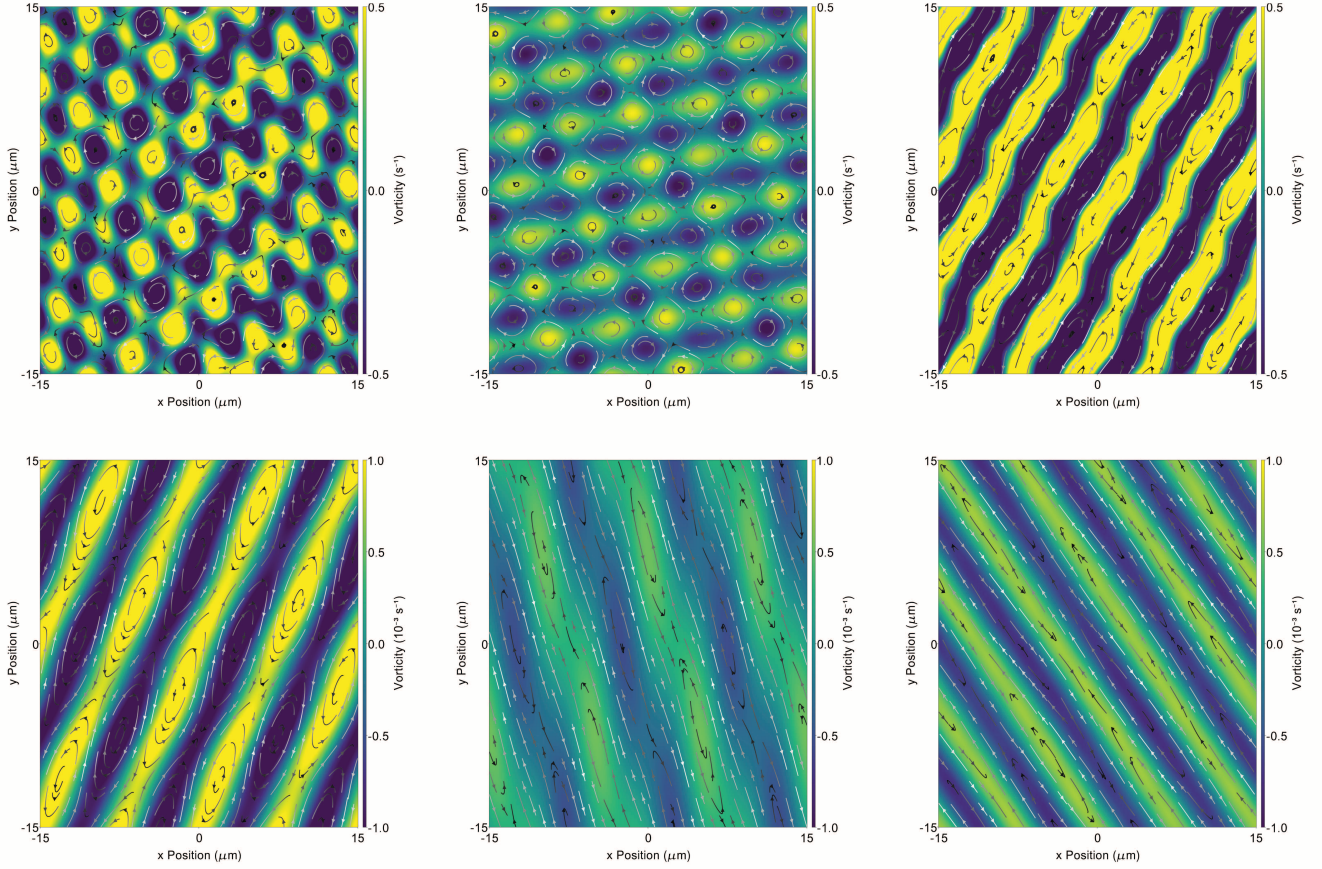


FIG. 7. Simulation snapshots of the vorticity Ω at $t = 0.16$ s for repeated trials of the condition $A = 20$ Pa (top row) and $A = -20$ Pa (bottom row). Each simulation was initially perturbed using a different random force field, giving rise to the observed variability in patterns.

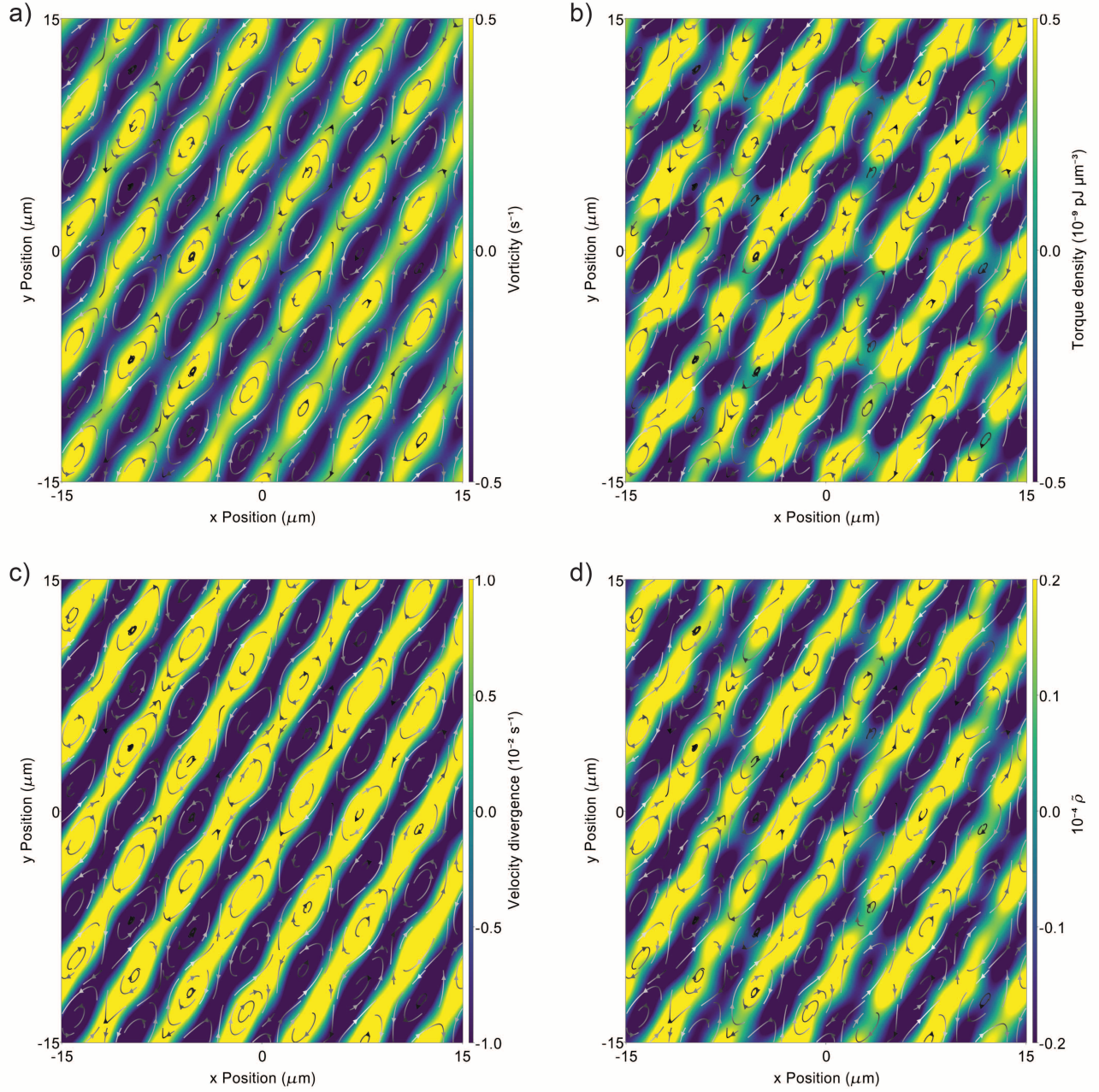


FIG. 8. Simulation snapshots of the vorticity $\partial_x v_y - \partial_y v_x$, viscoelastic torque density $\sigma_{xy}^p - \sigma_{yx}^p$, velocity divergence $\partial_k v_k$, and density variation $\tilde{\rho} = (\rho - \rho_s)/\rho_s$. These plots correspond to the same simulation at $t = 0.16$ s for $A = 20$ Pa, illustrating that similar spatial patterns have formed for each field.

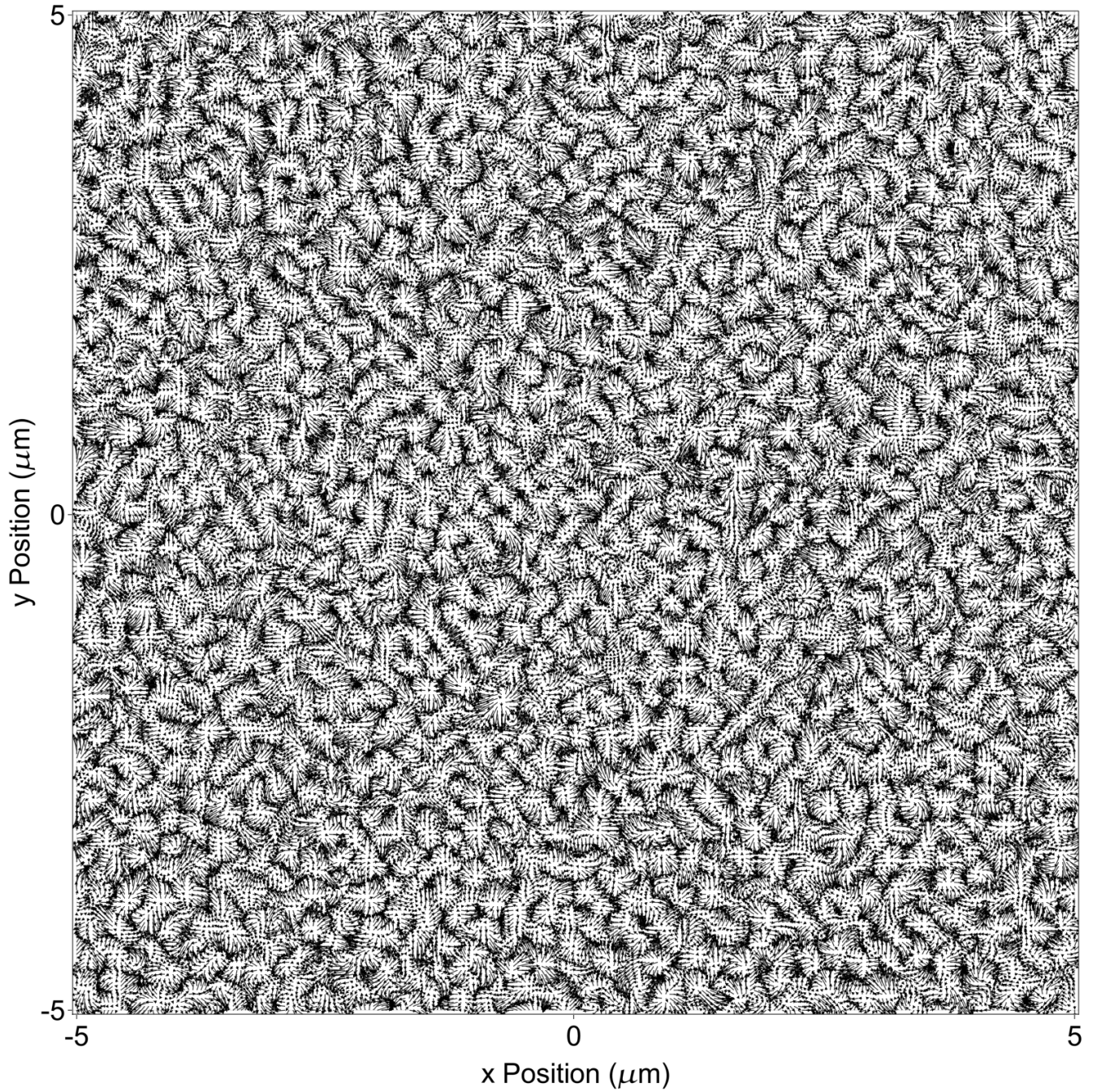


FIG. 9. An example vector field generated using Equations 26 and 27 is shown. Here, $N_x = N_y = 250$, $N_f = 300$, and $G = 40$. For the results reported in the paper, we take $G = 40$ when $N_x = N_y = 250$ and $G = 120$ when $N_x = N_y = 750$.

II. SUPPLEMENTARY METHODS

A. Derivation of odd viscoelastic instability threshold

Here we derive the linear stability conditions for excitations in an odd viscoelastic fluid.

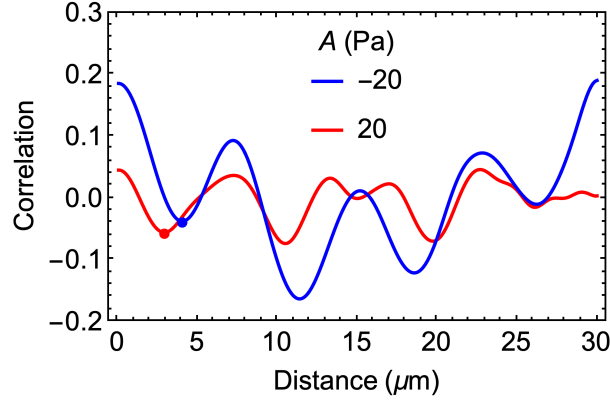


FIG. 10. For the simulation snapshots shown Figure 4c,d of the main text, we plot here the measured spatial correlation function of the vorticity field $\Omega(\mathbf{r})$. From these correlation functions, we take the position of the first minimum (shown as solid circles) a measure of half the spatial wavelength.

The dynamical equations governing the system are

$$\partial_t \rho = -\partial_j (\rho v_j) \quad (1)$$

$$p = c_s^2 \rho \quad (2)$$

$$\rho D_t v_i = -\partial_i p + \eta_s \partial_j (\partial_j v_i + \partial_i v_j) + \partial_j \sigma_{ij}^p \quad (3)$$

$$\mathcal{D}_t \sigma_{ij}^p = C_{ijkl} \partial_k v_l - \eta_p^{-1} C_{ijkl} \sigma_{kl}^p + D_p \partial_{kk} \sigma_{ij}^p. \quad (4)$$

See the main text for an explanation of the symbols in these equations. We have set the extra force density \mathbf{f} to zero here.

In principle the viscous response of the viscoelastic phase may also require a tensorial description $\eta_{p,ijkl}$, causing the second term in Equation 4 to depend on a tensor formed from the elasticity and viscosity tensors [1]. This generalization would not change the form of the dispersion relation derived below, but would require reinterpreting certain coefficients. We leave this extension to future work. We also note that one can straightforwardly consider the incompressible case of these dynamics by substituting p for ρ using Equation 2 in Equations 1 and 3 and taking the limit $c_s \rightarrow \infty$.

We first linearize the above equations around the uniform state $v_i^u = 0$, $\rho^u = \rho_s$, $\sigma_{ij}^u = 0$, such that $v_i = v_i'$, $\rho = \rho_s + \rho'$, and $\sigma_{ij} = \sigma_{ij}'$, where the primed variables are assumed small. The material and corotational derivatives reduce to partial derivatives to first order in the small variables. In what follows we drop the superscript p on the viscoelastic stress tensor, and we also drop the primes, with the understanding that all remaining variables are small. We eliminate the pressure from Equation 3 by substituting from Equation 2. The linearized set of equations is then

$$\partial_t \rho = -\rho_s \partial_i v_i \quad (5)$$

$$\rho_s \partial_t v_i = -c_s^2 \partial_i \rho + \eta_s (\partial_{jj} v_i + \partial_j \partial_i v_j) + \partial_j \sigma_{ij} \quad (6)$$

$$\partial_t \sigma_{ij} = -\eta_p^{-1} C_{ijkl} \sigma_{kl} + C_{ijkl} \partial_k v_l + D_p \partial_{kk} \sigma_{ij}. \quad (7)$$

Next we substitute the general form for the isotropic odd elastic tensor C_{ijkl} , which is shown in Ref. 2 to be

$$C_{ijkl} = B \delta_{ij} \delta_{kl} + \mu (\delta_{il} \delta_{jk} + \delta_{ik} \delta_{jl} - \delta_{ij} \delta_{kl}) + K^o E_{ijkl} - A \epsilon_{ij} \delta_{kl} \quad (8)$$

where

$$E_{ijkl} = \frac{1}{2} (\epsilon_{ik} \delta_{jl} + \epsilon_{il} \delta_{jk} + \epsilon_{jk} \delta_{il} + \epsilon_{jl} \delta_{ik}). \quad (9)$$

Here δ_{ij} is the Kronecker delta and ϵ_{ij} is the Levi-Civita tensor. Note that the expression for C_{ijkl} would be symmetric

in the indices i and j if not for the term proportional to A . With this, Equation 7 can be written as

$$\begin{aligned}\partial_t \sigma_{ij} = & -\eta_p^{-1} \left((B - \mu) \delta_{ij} \sigma_{kk} + \mu (\sigma_{ij} + \sigma_{ji}) - A \epsilon_{ij} \sigma_{kk} + \frac{K^o}{2} (\epsilon_{ik} \sigma_{kj} + \epsilon_{il} \sigma_{jl} + \epsilon_{jk} \sigma_{ki} + \epsilon_{jl} \sigma_{il}) \right) \\ & + (B - \mu) \delta_{ij} \partial_k v_k + \mu (\partial_j v_i + \partial_i v_j) - A \epsilon_{ij} \partial_k v_k + \frac{K^o}{2} (\epsilon_{ik} \partial_k v_j + \partial_j \epsilon_{ik} v_k + \epsilon_{jk} \partial_k v_i + \partial_i \epsilon_{jk} v_k) \\ & + D_p \partial_{kk} \sigma_{ij}.\end{aligned}\quad (10)$$

We next change to the following variables:

$$\Theta \equiv \partial_i v_i \quad (11)$$

$$\Omega \equiv \epsilon_{ij} \partial_i v_j \quad (12)$$

$$\sigma^I \equiv \sigma_{ii} \quad (13)$$

$$\sigma^{II} \equiv \partial_i \partial_j \sigma_{ij} \quad (14)$$

$$\sigma_L^{III} \equiv \epsilon_{ik} \partial_j \partial_k \sigma_{ij} \quad (15)$$

$$\sigma_R^{III} \equiv \epsilon_{jk} \partial_i \partial_k \sigma_{ij} \quad (16)$$

Our goal is now to express Equations 5, 6, and 7 in terms of these new variables. We divide this process into a few steps, as follows:

1. Take the time derivative of Equation 6. The result of this step is

$$\rho_s \partial_t^2 v_i = -c_s^2 \partial_i \partial_t \rho + \eta_s \partial_t (\partial_{jj} v_i + \partial_j \partial_i v_j) + \partial_j \partial_t \sigma_{ij}. \quad (17)$$

The expression for $\partial_t \sigma_{ij}$ can now be substituted from Equation 10.

2. Contract Equation 17 with ∂_i . This step produces an equation for the time evolution of Θ . After some algebra, we find

$$\begin{aligned}\rho_s \partial_t^2 \Theta = & -c_s^2 \partial_t \nabla^2 \rho + 2\eta_s \partial_t \nabla^2 \Theta \\ & - \eta_p^{-1} ((B - \mu) \nabla^2 \sigma^I + 2\mu \sigma^{II} - K^o (\sigma_R^{III} + \sigma_L^{III})) \\ & + (B + \mu) \nabla^2 \Theta + K^o \nabla^2 \Omega + D_p \nabla^2 \sigma^{II}.\end{aligned}\quad (18)$$

3. Contract Equation 17 with $\epsilon_{ki} \partial_k$. This step produces an equation for the time evolution of Ω . We find

$$\begin{aligned}\rho_s \partial_t^2 \Omega = & \eta_s \partial_t \nabla^2 \Omega \\ & + \eta_p^{-1} (\mu (\sigma_L^{III} + \sigma_R^{III}) - A \nabla^2 \sigma^I + K^o (2\sigma^{II} - \nabla^2 \sigma^I)) \\ & + \mu \nabla^2 \Omega + A \nabla^2 \Theta - K^o \nabla^2 \Theta - D_p \nabla^2 \sigma_L^{III}.\end{aligned}\quad (19)$$

4. Contract Equation 10 with δ_{ij} . This step produces an equation for the time evolution of σ^I . We find

$$\partial_t \sigma^I = -\eta_p^{-1} (B + \mu) \sigma^I + (B + \mu) \Theta + D_p \nabla^2 \sigma^I. \quad (20)$$

5. Contract Equation 10 with $\partial_i \partial_j$. This step produces an equation for the time evolution of σ^{II} . We find

$$\begin{aligned}\partial_t \sigma^{II} = & -\eta_p^{-1} ((B - \mu) \nabla^2 \sigma^I + 2\mu \sigma^{II} - K^o (\sigma_L^{III} + \sigma_R^{III})) \\ & + (B + \mu) \nabla^2 \Theta + K^o \nabla^2 \Omega + D_p \nabla^2 \sigma^{II}.\end{aligned}\quad (21)$$

6. Contract Equation 10 with $\epsilon_{ik} \partial_k \partial_j$. This step produces an equation for the time evolution of σ_L^{III} . We find

$$\begin{aligned}\partial_t \sigma_L^{III} = & -\eta_p^{-1} (\mu (\sigma_L^{III} + \sigma_R^{III}) - A \nabla^2 \sigma^I + K^o (2\sigma^{II} - \nabla^2 \sigma^I)) \\ & - \mu \nabla^2 \Omega - A \nabla^2 \Theta + K^o \nabla^2 \Theta + D_p \nabla^2 \sigma_L^{III}.\end{aligned}\quad (22)$$

7. Contract Equation 10 with $\epsilon_{jk}\partial_i\partial_k$. This step produces an equation for the time evolution of σ_R^{III} . We find

$$\begin{aligned}\partial_t\sigma_R^{III} = & -\eta_p^{-1}(\mu(\sigma_R^{III} + \sigma_L^{III}) + A\nabla^2\sigma^I + K^o(2\sigma^{II} - \nabla^2\sigma^I)) \\ & - \mu\nabla^2\Omega + A\nabla^2\Theta + K^o\nabla^2\Theta + D_p\nabla^2\sigma_R^{III}.\end{aligned}\quad (23)$$

We now have a collection of 7 equations, including $\partial_t\rho = -\rho_s\Theta$ from Equation 5, in 7 variables. Next, we consider plane wave perturbations corresponding to the ansatz

$$\Theta(\mathbf{r}, t) \sim \Theta(\mathbf{k}, \omega)e^{\nu t}e^{i\mathbf{k}\cdot\mathbf{r}} \quad (24)$$

and convert the differential equations into algebraic equations in the Fourier coefficients. After this, we collect everything into the following matrix equation:

$$\begin{pmatrix} \nu & \rho_s & 0 & 0 & 0 & 0 & 0 \\ c_s^2k^2\nu & -k^2H_+ - 2k^2\eta_s\nu - \rho_s\nu^2 & -k^2K^o & \frac{k^2H_-}{\eta_p} & -k^2D_p - \frac{2\mu}{\eta_p} & \frac{K^o}{\eta_p} & \frac{K^o}{\eta_p} \\ 0 & -k^2G_- & -\rho_s\nu^2 - k^2(\mu + \eta_s\nu) & \frac{k^2G_+}{\eta_p} & \frac{2K^o}{\eta_p} & D_pk^2 + \frac{\mu}{\eta_p} & \frac{\mu}{\eta_p} \\ 0 & H_+ & 0 & -\frac{B_+F_1}{\eta_p} & 0 & 0 & 0 \\ 0 & -k^2H_+ & -k^2K^o & \frac{k^2H_-}{\eta_p} & -\frac{F_2}{\eta_p} & \frac{K^o}{\eta_p} & \frac{K^o}{\eta_p} \\ 0 & k^2G_- & k^2\mu & -\frac{k^2G_+}{\eta_p} & -\frac{2K^o}{\eta_p} & -\frac{F_1}{\eta_p} & -\frac{\mu}{\eta_p} \\ 0 & -k^2G_+ & k^2\mu & \frac{k^2G_-}{\eta_p} & -\frac{2K^o}{\eta_p} & -\frac{\mu}{\eta_p} & -\frac{F_1}{\eta_p} \end{pmatrix} \begin{pmatrix} \rho \\ \Theta \\ \Omega \\ \sigma^I \\ \sigma^{II} \\ \sigma_L^{III} \\ \sigma_R^{III} \end{pmatrix} = 0, \quad (25)$$

where $F_1 \equiv D_pk^2\eta_p + \mu + \eta_p\nu$, $F_2 \equiv D_pk^2\eta_p + 2\mu + \eta_p\nu$, $G_{\pm} \equiv A \pm K^o$, and $H_{\pm} \equiv B \pm \mu$.

Finally, the dispersion relation $\nu(k)$ is obtained as the solution of $\det(\mathcal{M}) = 0$, where \mathcal{M} is the matrix in Equation 25. This equation has 9 solutions which, without any further assumptions, are highly complicated. We do not write them here, but we note that they reduce to the results derived in Ref. 3 for the special case $\eta_s = 0$, $\eta_p \rightarrow \infty$, $D_p = 0$, and $A = 0$.

B. Simulation methods

1. Numerical algorithm

To numerically solve the dynamical equations of the odd Jeffrey fluid, we rely on the hybrid lattice Boltzmann (HLB) method using the $d2Q9$ lattice [4]. This technique uses a combination of the lattice Boltzmann method to update the velocity and density fields $\mathbf{v}(\mathbf{r})$ and $\rho(\mathbf{r})$, and a finite difference integration scheme to update the polymer orientation vector field $\mathbf{P}(\mathbf{r})$ and the viscoelastic stress tensor field $\boldsymbol{\sigma}^p(\mathbf{r})$. Periodic boundary conditions are used for all fields.

2. Initial perturbation

To numerically study pattern formation we apply a small initial perturbation to the fluid to excite the instability. This is done through the external body force field \mathbf{f}_{ext} which is included as a contribution to the force density \mathbf{f} in Equation 3 of the main text. Specifically, we apply a force of the form $\mathbf{f}_{\text{ext}}(\mathbf{r}, t) = T(t)\mathbf{F}^f(\mathbf{r})$, where $T(t)$ is a smooth bump function formed from sigmoidal curves that sets the magnitude of the force field, and $\mathbf{F}^f(\mathbf{r})$ is a normalized vector field. For the vector field, we use

$$F_x^f(x, y) = \frac{1}{H} \sum_{i=1}^{N_f} \left(a_i^{\text{cx}} \cos(b_i^{\text{cx}}l_x x + c_i^{\text{cx}}l_y y) + a_i^{\text{sx}} \sin(b_i^{\text{sx}}l_x x + c_i^{\text{sx}}l_y y) \right) \quad (26)$$

$$F_y^f(x, y) = \frac{1}{H} \sum_{i=1}^{N_f} \left(a_i^{\text{cy}} \cos(b_i^{\text{cy}}l_x x + c_i^{\text{cy}}l_y y) + a_i^{\text{sy}} \sin(b_i^{\text{sy}}l_x x + c_i^{\text{sy}}l_y y) \right) \quad (27)$$

where $l_x = 2\pi/N_x$ and $l_y = 2\pi/N_y$. The random numbers a_i^{cx} , a_i^{cy} , a_i^{sx} , and a_i^{sy} are drawn from a normal distribution with mean 0 and variance 1. The random numbers b_i^{cx} , c_i^{cx} , b_i^{sx} , c_i^{sx} , b_i^{cy} , c_i^{cy} , b_i^{sy} , and c_i^{sy} are drawn from a discrete uniform distribution over the domain $[-G, G]$, with the integer G chosen as 120 for the grid size $N_x = N_y = 750$ and 40 for the grid size $N_x = N_y = 250$. We take $N_f = 300$ and then normalize $\mathbf{F}^f(\mathbf{r})$ by choosing H so that the largest vector in the field has unit norm. The magnitude $T^f(t)$ is kept at 10^{-8} (in lattice units) for the first 150 timesteps of the simulation, with a sigmoidal width of 30 timesteps.

The rationale behind this choice of perturbation is that it has the following desirable properties:

- It is approximately isotropic, not preferring any direction in the grid.
- When G is large it allows for a wide range of spatial frequencies to be excited, increasing the chances that the fastest growing mode of the instability will be excited.
- It obeys the periodic boundary conditions, avoiding a large gradient at the boundary due to a discontinuity.

An example of a vector field generated using this method is visualized in Figure 9.

3. Parameterization

Roughly, the system we have in mind is a micron-scale aqueous viscoelastic solution with elastic moduli on the order of a few Pa, corresponding to the cytoplasm. Experimentally verified parameter values, such as the viscosity of water, were used wherever possible. Several parameters were instead treated as free rather than constrained by experiments. The values reported in the tables below are the defaults, so when a given parameter is varied the remaining parameters are set to these values. We note that, following standard practice with LB simulations, the density of water is set to several orders of magnitude larger than its actual value [5–8]. This allows increasing the time step (thereby speeding up simulations) while still ensuring that the system has a small Reynolds number. We refer the reader to Ref. 9 for a full description of all parameters listed below.

Parameter	Symbol	Value
Lattice spacing	Δx	4×10^{-8} m
Timestep	Δt	8×10^{-6} s
Number of steps	N_{steps}	25,000, 200,000
Collision operator time	τ	1.25
Solvent dynamic viscosity	η_s	0.001 Pa s
Solvent density	ρ_s	2×10^7 kg/m ³
Lattice size	$N_x = N_y$	250, 750

TABLE I. Default parameters used in simulation related to the LB algorithm and system domain are shown. These parameters were used to generate the data on the pattern forming instability.

Parameter	Symbol	Value
Polymeric viscosity	η_p	0.1 Pa s
Stress diffusion constant	D_p	10^{-13} m ² /s
Isotropic stiffness tensor element	B	5.0 Pa
Isotropic stiffness tensor element	A	5.0 Pa
Isotropic stiffness tensor element	K^o	5.0 Pa
Isotropic stiffness tensor element	μ	2.0 Pa

TABLE II. Default parameters used in simulation related to the viscoelastic stress are shown. These parameters were used to generate the data on the pattern forming instability.

4. Measuring the wavelength

To systematically estimate the length scale of the pattern as conditions are varied, we analyze the spatial correlation $C_\Omega(d)$ of the vorticity field $\Omega(\mathbf{r})$. We first normalize Ω so that its maximum value over the grid is 1. We then estimate

$C_\Omega(d)$ as

$$C_\Omega(d) = \frac{\sum_{i,j=1}^{N_x, N_y} \delta(|i-j|-d) (\Omega_{ii}\Omega_{ij} + \Omega_{ii}\Omega_{ji})}{2 \sum_{i,j=1}^{N_x, N_y} \delta(|i-j|-d)} \quad (28)$$

where $\delta(d)$ is the Kronecker delta function, and Ω_{ij} is value of Ω at the i, j lattice point. This formula estimates $C_\Omega(d)$ by evaluating it for reference points along the main diagonal of the grid. The argument $d = r/\Delta x$ is in lattice units but can be converted to physical units using the simulation length scale Δx .

For the periodic vortex arrays that make up the typical patterns observed in simulation, the correlation function $C_\Omega(d)$ is also roughly periodic (Figure 10). To estimate the wavelength of the array, we pick the value of d where $C_\Omega(d)$ attains its first minimum. This value of d is then interpreted as half of the pattern's wavelength.

III. A MICROSCOPIC DERIVATION OF THE VISCOELASTIC DYNAMICAL EQUATIONS

Here we consider a tractable microscopic system, a “non-reciprocal elastic dumbbell” model, and coarse-grain it following standard procedures to show how new “odd” terms emerge alongside those which appear in the usual upper-convected Maxwell model. This derivation does not reproduce the exact dynamical equations of the odd Jeffreys fluid considered in this paper, which requires a more detailed microscopic model and is left to future work. However, it does indicate how some new terms which are found in the odd Jeffreys dynamics arise from non-reciprocal interactions at the microscopic level.

Our derivation primarily follows Refs. 10 and 11, and we consider a 2D system. The standard elastic dumbbell model was introduced by Kuhn [12] and describes a solution of polymers whose endpoints behave as if connected by a harmonic spring. The interactions between the polymer and the solvent are localized at these endpoints, which are at \mathbf{r}_+ , \mathbf{r}_- and are governed by overdamped Langevin dynamics. The separation vector $\mathbf{R} \equiv \mathbf{r}_+ - \mathbf{r}_-$ and center-of-mass position $\mathbf{R}^c = \frac{1}{2}(\mathbf{r}_+ + \mathbf{r}_-)$ obey, to second order in the solvent velocity \mathbf{u}^c evaluated at \mathbf{R}^c ,

$$\partial_t R_i^c = u_i^c + \frac{1}{8} R_j R_k \partial_j \partial_k u_i^c + \zeta^{-1} F_i^{b,c}(t), \quad (29)$$

$$\partial_t R_i = (\partial_j u_i^c) R_j + 2\zeta^{-1} F_i^{\text{int}} + \zeta^{-1} F_i^b(t). \quad (30)$$

Here, ζ is a scalar friction coefficient obeying the fluctuation-dissipation relation with the Brownian forces $\mathbf{F}^{b,c}$ and \mathbf{F}^b which act, respectively, on \mathbf{R}^c and \mathbf{R} :

$$\langle F_i^{b,c}(t) \rangle = 0, \quad \langle F_i^{b,c}(t+t') F_j^{b,c}(t) \rangle = k_B T \zeta \delta(t') \delta_{ij}, \quad (31)$$

$$\langle F_i^b(t) \rangle = 0, \quad \langle F_i^b(t+t') F_j^b(t) \rangle = 4k_B T \zeta \delta(t') \delta_{ij}. \quad (32)$$

In the standard elastic dumbbell model, the interaction force is

$$F_i^{\text{int}} = -k_{\parallel} R_i, \quad (33)$$

i.e., the polymer behaves like a harmonic spring with zero rest length. We add to this interaction a transverse force depending on the separation \mathbf{R} :

$$F_i^{\text{int}} = -k_{\parallel} R_i - k_{\perp} \epsilon_{ij} R_j = -M_{ij} R_j, \quad (34)$$

where

$$M_{ij} = k_{\parallel} \delta_{ij} + k_{\perp} \epsilon_{ij}. \quad (35)$$

We seek the evolution of the quantity $\langle R_i R_j \rangle$, which we will eventually relate to the viscoelastic stress tensor σ_{ij}^P . Using Equation 30, we have

$$\partial_t (R_i R_j) = (\partial_k u_i^c) R_k R_j + R_i R_k (\partial_k u_j^c) + 2\zeta^{-1} (F_i^{\text{int}} R_j + F_j^{\text{int}} R_i) + \zeta^{-1} (F_i^b(t) R_j + F_j^b(t) R_i). \quad (36)$$

In expectation, the Brownian force terms can be simplified using a separation of timescales between R_i and $F_i^b(t)$ [10]:

$$\langle R_i F_j^b \rangle \approx \langle F_i^b R_j \rangle \approx 2k_B T \delta_{ij}. \quad (37)$$

The interaction terms can be expressed as

$$F_i^{\text{int}} R_j + F_j^{\text{int}} R_i = -M_{ik} R_k R_j - R_i M_{jk} R_k = -\tilde{C}_{ijkl} R_k R_l \quad (38)$$

where

$$\tilde{C}_{ijkl} = M_{ik} \delta_{jl} + M_{jk} \delta_{il} \quad (39)$$

$$= k_{\parallel} (\delta_{ik} \delta_{jl} + \delta_{jk} \delta_{il}) + \frac{k_{\perp}}{2} (\epsilon_{ik} \delta_{jl} + \epsilon_{il} \delta_{jk} + \epsilon_{jk} \delta_{il} + \epsilon_{jl} \delta_{ik}). \quad (40)$$

This tensor is of the same form as Equation 8 above, when $B = \mu$ and $A = 0$. We note that the symmetrized combinations $(\epsilon_{ik} \delta_{jl} + \epsilon_{il} \delta_{jk})/2$ and $(\epsilon_{jk} \delta_{il} + \epsilon_{jl} \delta_{ik})/2$ appear because the contraction with $R_k R_l$ should be symmetric under the interchange of indices k and l . The expectation of Equation 36 can now be written as

$$\partial_t \langle R_i R_j \rangle = (\partial_k u_i^c) \langle R_k R_j \rangle + \langle R_i R_k \rangle (\partial_k u_j^c) - 2\zeta^{-1} \tilde{C}_{ijkl} \langle R_k R_l \rangle + 4k_B T \zeta^{-1} \delta_{ij}. \quad (41)$$

The polymer-contributed stress can be written as $S_{ij}^p = (1/2)\nu \tilde{C}_{ijkl} \langle R_k R_l \rangle$ where ν is the number density of polymers. Contracting both sides of Equation 41 with $\nu \tilde{C}_{ijkl}$ and using the upper convected derivative $\mathcal{D}_t^{\text{uc}} X_{ij} = \partial_t X_{ij} - (\partial_k u_i^c) X_{kj} - X_{ik} (\partial_k u_j^c)$, we have

$$\nu \tilde{C}_{ijkl} \mathcal{D}_t^{\text{uc}} \langle R_k R_l \rangle = -4\zeta^{-1} \tilde{C}_{ijkl} S_{kl}^p + 4k_B T \nu \zeta^{-1} \tilde{C}_{ijkl} \delta_{kl}. \quad (42)$$

The operations of $\mathcal{D}_t^{\text{uc}}$ and contraction with \tilde{C}_{ijkl} do not commute when $k_{\perp} \neq 0$. However, since we are interested in the linear stability regime, for simplicity, we neglect the commutator of these operations, which is second order in the perturbations around the homogeneous state. It is standard to redefine the polymer stress to absorb the pressure-like term: $\sigma_{ij}^p = S_{ij}^p - k_B T \nu \delta_{ij}$. With this, we can write

$$\mathcal{D}_t^{\text{uc}} S_{ij}^p = \mathcal{D}_t^{\text{uc}} \sigma_{ij}^p + k_B T \nu \mathcal{D}_t^{\text{uc}} \delta_{ij} = -2\zeta^{-1} \tilde{C}_{ijkl} \sigma_{kl}^p. \quad (43)$$

One can show that $\mathcal{D}_t^{\text{uc}} \delta_{ij} = -(\partial_i u_j^c + \partial_j u_i^c) = -2\Psi_{ij}$, so that

$$\mathcal{D}_t^{\text{uc}} \sigma_{ij}^p = 2k_B T \nu \Psi_{ij} - 2\zeta^{-1} \tilde{C}_{ijkl} \sigma_{kl}^p. \quad (44)$$

If $k_{\perp} = 0$, then Equation 44 reduces to the standard upper convected Maxwell model:

$$\mathcal{D}_t^{\text{uc}} \sigma_{ij}^p = 2k_B T \nu \Psi_{ij} - 4k_{\parallel} \zeta^{-1} \sigma_{ij}^p. \quad (45)$$

Defining the relaxation time $\lambda = \zeta/4k_{\parallel}$ and thermal energy density $G = \nu k_B T$, this can be expressed in the familiar form

$$\lambda \mathcal{D}_t^{\text{uc}} \sigma_{ij}^p = 2\tilde{\eta}_p \Psi_{ij} + \sigma_{ij}^p \quad (46)$$

where $\tilde{\eta}_p = G\lambda$. If the polymeric elasticity is due to the Kuhn stiffness of a Gaussian chain, we can write

$$k_{\parallel} = a k_B T, \quad (47)$$

where the proportionality a (having units of inverse length squared) is related to the Kuhn length and the number of Kuhn segments. By assuming a similar relationship between stiffness \tilde{C}_{ijkl} and thermal energy for the case when $k_{\perp} \neq 0$, we generalize the coefficient of Ψ_{ij} in Equation 44 so that it reads

$$\mathcal{D}_t^{\text{uc}} \sigma_{ij}^p = \frac{2\nu}{a} \tilde{C}_{ijkl} \Psi_{ij} - 2\zeta^{-1} \tilde{C}_{ijkl} \sigma_{kl}^p. \quad (48)$$

Defining $C_{ijkl} = \frac{2\nu}{a} \tilde{C}_{ijkl}$ and $\eta_p = \zeta\nu/a$, we can write

$$\mathcal{D}_t^{\text{uc}} \sigma_{ij}^p = C_{ijkl} \Psi_{ij} - \eta_p^{-1} C_{ijkl} \sigma_{kl}^p. \quad (49)$$

This last equation can be compared to Equation 4, and σ_{ij}^p can be added to the solvent phase stresses to give the final Navier-Stokes equation for the Oldroyd-B fluid. An Oldroyd-B fluid, which is the same as a Jeffrey fluid but with an upper-convected rather than co-rotational derivative in the evolution for the viscoelastic stress tensor, is a model for a viscoelastic Maxwell material immersed in a viscous solvent. The two components are assumed to flow together, and thus one velocity field suffices to describe the motion of the combined system. The two components however make separate additive contributions to the total stress tensor, which enters the momentum-balance encoded in the Navier-Stokes equation. This physical approximation to the two-component system of polymer and solvent is quite standard in rheology, and models like the Jeffrey fluid have successfully reproduced numerous experimental observations [10, 11, 13]. We note that in certain situations this model suffers from physically inconsistent singularities owing to the assumed infinite extensibility of the constituent polymers. For our linear instability calculations this issue is not important.

The derivation presented here does not exactly reproduce Equation 4, missing some terms in the elasticity tensor and using a different materially objective derivative, but it illustrates how the odd coefficient K^o in the elasticity tensor, which drives instabilities, arises from microscopic forces proportional to k_\perp . Future work could focus on a similar derivation of viscoelastic dynamics from spinning colloids, rather than from a polymeric system with transverse forces as considered here.

-
- [1] Debarghya Banerjee, Vincenzo Vitelli, Frank Jülicher, and Piotr Surówka. Active viscoelasticity of odd materials. *Physical Review Letters*, 126(13):138001, 2021.
 - [2] Colin Scheibner, Anton Souslov, Debarghya Banerjee, Piotr Surówka, William Irvine, and Vincenzo Vitelli. Odd elasticity. *Nature Physics*, 16(4):475–480, 2020.
 - [3] Shiladitya Banerjee, Margaret L Gardel, and Ulrich S Schwarz. The actin cytoskeleton as an active adaptive material. *Annual Review of Condensed Matter Physics*, 11:421–439, 2020.
 - [4] Livio Nicola Carenza, Giuseppe Gonnella, Antonio Lamura, Giuseppe Negro, and Adriano Tiribocchi. Lattice Boltzmann methods and active fluids. *The European Physical Journal E*, 42(6):1–38, 2019.
 - [5] Elsen Tjhung, Davide Marenduzzo, and Michael E Cates. Spontaneous symmetry breaking in active droplets provides a generic route to motility. *Proceedings of the National Academy of Sciences*, 109(31):12381–12386, 2012.
 - [6] ME Cates, K Stratford, R Adhikari, P Stansell, JC Desplat, I Pagonabarraga, and AJ Wagner. Simulating colloid hydrodynamics with lattice Boltzmann methods. *Journal of Physics: Condensed Matter*, 16(38):S3903, 2004.
 - [7] K Wolff, D Marenduzzo, and ME Cates. Cytoplasmic streaming in plant cells: the role of wall slip. *Journal of the Royal Society Interface*, 9(71):1398–1408, 2012.
 - [8] Oliver Henrich, Kevin Stratford, Davide Marenduzzo, and Michael E Cates. Ordering dynamics of blue phases entails kinetic stabilization of amorphous networks. *Proceedings of the National Academy of Sciences*, 107(30):13212–13215, 2010.
 - [9] Carlos Floyd, Suriyanarayanan Vaikuntanathan, and Aaron R Dinner. Simulating structured fluids with tensorial viscoelasticity. *Journal of Chemical Physics*, 158(5):054906, 2023.
 - [10] Nhan Phan-Thien and Nam Mai-Duy. *Understanding viscoelasticity: an introduction to rheology*. Springer, 2013.
 - [11] Ronald G Larson. *Constitutive Equations for Polymer Melts and Solutions*. Butterworth-Heinemann, 2013.
 - [12] Werner Kuhn. Über die gestalt fadenförmiger moleküle in lösungen. *Kolloid-Zeitschrift*, 68:2–15, 1934.
 - [13] Robert Byron Bird, Robert Calvin Armstrong, and Ole Hassager. *Dynamics of Polymeric Liquids. Vol. 1: Fluid Mechanics*. John Wiley and Sons Inc., New York, NY, 1987.